communications physics

ARTICLE

https://doi.org/10.1038/s42005-023-01261-6 OPEN

Variable-order topological insulators

Yating Yang[1], Handa Sun[2], Jiuyang Lu[2], Xueqin Huang[2], Weiyin Deng[2✉] & Zhengyou Liu[3,4✉]

Topological insulators, either the first-order or the higher-order, experience generally a transition to a trivial phase or a topological one of the same order through the gap closing and reopening procedure. Here, we report a topological insulator, which switches directly between the first and higher orders, with only varying the hoppings and without breaking the symmetry. The phase transition of the first and higher orders is originated from a competition mechanism between the nearest and second-nearest neighbor interactions. This variable-order topological insulator is implemented in a two-dimensional phononic crystal, and the one-dimensional helical edge states, which signal the first-order phase, and the zero-dimensional corner states, which signal the second-order one, are demonstrated in the simulations and experiments. Our study gives insight to the topological states of different orders.

[1] College of Mathematics and Physics, Beijing University of Chemical Technology, 100029 Beijing, China. [2] School of Physics and Optoelectronics, South China University of Technology, 510640 Guangzhou, China. [3] Key Laboratory of Artificial Micro- and Nanostructures of Ministry of Education and School of Physics and Technology, Wuhan University, 430072 Wuhan, China. [4] Institute for Advanced Studies, Wuhan University, 430072 Wuhan, China. ✉email: dengwy@scut.edu.cn; zyliu@whu.edu.cn

Topological phases, including the conventional first-order and higher-order topological insulators (TIs), have attracted wide attention in electronic[1,2], photonic[3], and phononic[4,5] materials. Generally, d-dimensional (dD) conventional first-order TIs possess $(d-1)$D topological boundary states. There exist two types of the two-dimensional (2D) first-order TIs, featured with the 1D edge states. The first type hosts the chiral edge states and thus breaks the time-reversal symmetry, and is commonly called Chern insulator, whose topological invariant is the Chern number[6,7]. The second type possesses the helical edge states, and can classified by the Z_2 index or spin-Chern numbers, such as the quantum spin Hall insulator[8,9] and spin-Chern insulator (SCI)[10,11]. The quantum spin Hall insulator has the gapless edge states protected by the spin-1/2 electronic time-reversal operator. The SCI extends the concept of quantum spin Hall insulator, which has the helical edge states, but their gapless properties rely on the symmetry and boundary potential of the sample[12]. By tuning the alternating sublattice potential, it has been found that these 2D first-order TIs can be transited to the trivial normal insulator (NI)[7,8,10]. Importantly, a topological phase transition from the SCI to Chern insulator occurs in the presence of the Zeeman field, providing a practical way to realize the Chern insulator[10,13–15].

Higher-order topological phases generalize the conventional bulk-boundary correspondence[16–20], in which dD nth-order ($n>1$) TIs have $(d-n)$D topological boundary states. The 2D second-order TIs (SOTIs) are characterized by the 0D in-gap corner states[21], which can be originated from the quantized quadrupole moments[20], the quantized bulk polarizations[22] and the Jackiw-Rebbi mechanism[23]. The corner states have been observed in the artificial periodical structures, including the photonic crystals[24–27], phononic crystals (PCs)[28–32] and electric circuits[33–35], thanks to their macroscopic nature. The corner states are further explored to exhibit the helical[36], pseudospin-dependent[37,38] and valley-selective[39] properties. While breaking or reducing an essential symmetry, the first-order TIs can be transited to the higher-order TIs[16,23,40–46], which to realize the higher-order topological phases. For example, while breaking the time-reversal symmetry, the quantum spin Hall insulator can open an edge gap and host the in-gap corner state, transiting to a SOTI[42–44]. The recently proposed[45] and realized[46] Dirac hierarchy in 3D acoustic topological insulators provides another concrete example to achieve the topological transitions between the first-order, second-order and third-order TIs by step-by-step breaking different symmetries. A natural question is that whether the topological phase transition occurs between the higher-order and first-order TIs without breaking the symmetry.

In this work, we answer this question and realize a topological phase, referred as the variable-order TI, which switches directly between the first and higher orders, with only varying the hoppings and without breaking the symmetry. We first construct the tight-binding model of a bilayer kagome lattice, where two different intralayer nearest-neighbor hoppings can induce SOTI phase originated from quantized bulk polarizations, and a chiral interlayer hopping may give rise to SCI phase. The competition between these two couplings leads to the topological phase transition between SCI and SOTI phases. Then we map the lattice model to PC and find that the phase transition occurs with changing structural parameter but keeping the symmetry. A pair of 1D helical edge states in the SCI phase and 0D corner states in the SOTI phase are demonstrated in the simulations and experiments with good agreement.

Results

Tight-binding model for variable-order TI. We start from the bilayer kagome lattice model with three inequivalent sites labeled as 1–3 in each layer, as shown in Fig. 1a, where gray circles denote the sites, blue (red) line denote the nearest-neighbor (NN) hopping t_0-d_t (t_0+d_t), and green line denote chiral interlayer coupling with hopping integral t_b. The tight-binding model can be written as

$$H=\sum_{<ij>,\alpha} t_p c_{i\alpha}^{\dagger}c_{j\alpha}+t_b\sum_{\ll ij\gg,\alpha\neq\beta} v_{ij,\alpha}c_{i\alpha}^{\dagger}c_{j\beta}. \quad (1)$$

Here, the first term is the NN intralayer hopping with $c_{i\alpha}^{\dagger}$ as the creation operator of layer pseudospin α on site i, and the hopping integral $t_p=t_0-d_t$ (t_0+d_t) when the bond between i and j lives in (out) the unit cell. The second term is interlayer interactions, where $v_{ij,\alpha}=\frac{1}{2}\left[1+\frac{8}{\sqrt{3}}v_\alpha(\hat{e}_{jk}\times\hat{e}_{ki})_z\right]$ describes the relationship between the hopping directions of the next-nearest neighbor couplings and the symbol of pseudospins $v_{\uparrow\downarrow}=\pm1$. k is the common NN site between sites i and j, and $\hat{e}_{jk}$ is the unit vector pointing from j to k. In our model, $v_{ij,\alpha}$ is equal to 0 or 1. $v_{ij,\alpha}=0$ means that there is no interlayer coupling connection between the two next-nearest lattice points, and $v_{ij,\alpha}=1$ means that there is interlayer coupling connection between the two next-nearest lattice points. t_0 is set to -1, and the lattice constant is set to unity with $\boldsymbol{a}_1=\hat{x}$ and $\boldsymbol{a}_2=\left(\hat{x}+\sqrt{3}\hat{y}\right)/2$. The interlayer coupling can induce the pseudospin-orbit interaction and may give rise to the SCI phase[11], while the intralayer ones may result in the SOTI phase with quantized bulk polarizations[22]. So the competition of the interlayer and intralayer couplings can result in the topological phase transition between the SCI and SOTI phases.

We then calculate the topological invariants of the system. The Brillouin zone with high symmetry points is shown in Fig. 1b, where the red rhombic denotes the first Brillouin zone to form a closed loop to calculate the topological invariants. k_1 and k_2 are the wavevector components along the directions of the reciprocal lattice vectors. The topological phase as functions of t_b/t_0 and d_t/t_0 is illustrated in Fig. 1c. The topological properties of the SCI phase can be described by the spin-Chern numbers $C_\pm$, while the SOTI is characterized by the spin-polarized bulk polarizations $P_{1\pm}$ and $P_{2\pm}$, which are equal due to the C_3 symmetry. There are three different phases, SCI with $C_\pm=\pm1$ in the pink area, SOTI with $C_\pm=0$ and $P_{1\pm}=-1/3$ in the purple area, and NI with $C_\pm=0$ and $P_{1\pm}=0$ in the blue area (see Supplementary Note 1). The boundaries of these phases are formed by the critical points with the bulk gap closure between the second and third bands, which can be analytically obtained as $d_t/t_b=\pm2/3$, plotted by the white lines.

In Fig. 1d, fixed $t_b/t_0=0.6$, bulk dispersions with $d_t/t_0=-0.3$ (point A), $d_t/t_0=0.4$ (point B), $d_t/t_0=0.8$ (point C) are depicted. SCI gap marked by pink area is reduced to a degenerate point, and then reopened as a SOTI gap marked by purple area. The boundary states revealing the SCI and SOTI phases will emerge in the nontrivial band gaps according to the bulk-boundary correspondence. For parameters at point A, the projected dispersion of a ribbon with open boundary along the y direction is shown in Fig. 1e. One can see that a pair of the helical edge states, located at the top (green lines) and bottom (red lines) boundaries, exist in the bulk gap, demonstrating the point A hosts the SCI phase. For parameters at point C, the energy spectrum of 5 layers triangle-shaped sample is plotted in Fig. 1f. Point C is the SOTI phase, possessing six corner states at zero-energy labeled by orange circles, in which a pair of the corner states localize at a corner and are protected by the C_2 symmetry.

Acoustic variable-order TI. Next, we discuss the realization of the above topological phase transitions in a PC. The unit cell of the PC is shown in Fig. 2a with $a=5$mm. The cylindrical cavities

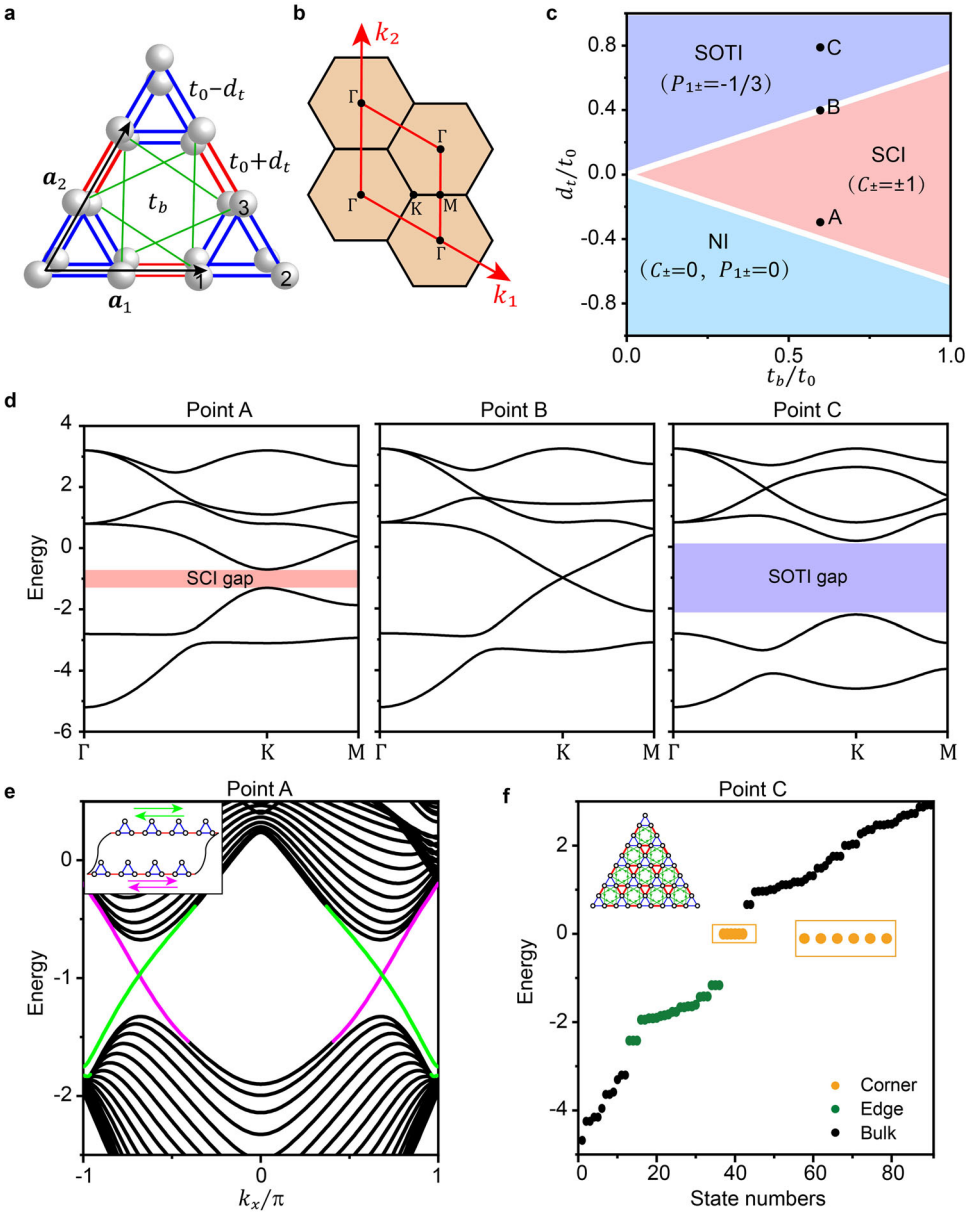

Fig. 1 Variable-order topological insulator with phase transition between the spin-Chern insulator (SCI) and second-order topological insulator (SOTI). a Bilayer breathing kagome lattice model with three inequivalent sites (gray circles) labeled as 1-3 in each layer of a unit cell. Blue (red) line denotes the NN intralayer hopping $t_0 - d_t$ ($t_0 + d_t$). Green line denotes the chiral interlayer hopping t_b. **b** The first Brillouin zone (red rhombic) with high symmetry points. **c** Phase diagram in the t_b/t_0 versus d_t/t_0 plane. White lines are the phase boundaries with bulk gap closure. Normal insulator in the phase diagram is abbreviated as NI. **d** Bulk dispersions with $d_t/t_0 = -0.3$ (point A), $d_t/t_0 = 0.4$ (point B), $d_t/t_0 = 0.8$ (point C). **e** Projected dispersions of a ribbon with open boundary along the *y* direction for parameters at point A in (**c**). Inset: the illustrations of the ribbon and the edge states propagations. **f** Eigenvalue of a triangle-shaped sample (inset) for parameters at point C.

can be viewed as the lattice sites, with the diameter $d_c = 12.2$mm and height $h_c = 26.5$mm. Left panel shows a top view of the three cavities clearly on each layer and two different types of tubes (diameter $d_0 \pm d_r$ with $d_0 = 2.5$mm) connecting the NN cavities provide the different intralayer couplings. Right panel with a side view clearly shows the chiral interlayer tubes (diameter $d_b = 2.6$mm) connect the cavities between the upper and lower layers, giving rise to the interlayer couplings. Since we focus on the bands of the dipole mode, two parallel tubes are used to connect the cavities at the heights of $h_c/4$ and $3h_c/4$ in each layer, and the interlayer tubes connect the bottom of the cavities of the upper layer with the top of the ones of the lower layer. As such, the PC is consistent with the lattice model described by Eq. (1).

The phase diagram of dipole modes as a function of d_r/d_0 is shown in Fig. 2b, where the lower (upper) line denotes the top (bottom) of the second (third) band of dipole mode. There are three topologically distinct phases, i.e., the NI (blue area), SCI (pink area) and SOTI (purple area), corresponding to the lattice model. The phase transition points are at $d_r/d_0 = -0.29$ and 0.29 with bulk gap closing (the gray dashed lines). As shown in Fig. 2c, the bulk dispersion of dipole modes is gapless at *K* point (the red dashed line) for $d_r/d_0 = 0.29$. The bulk dispersions of

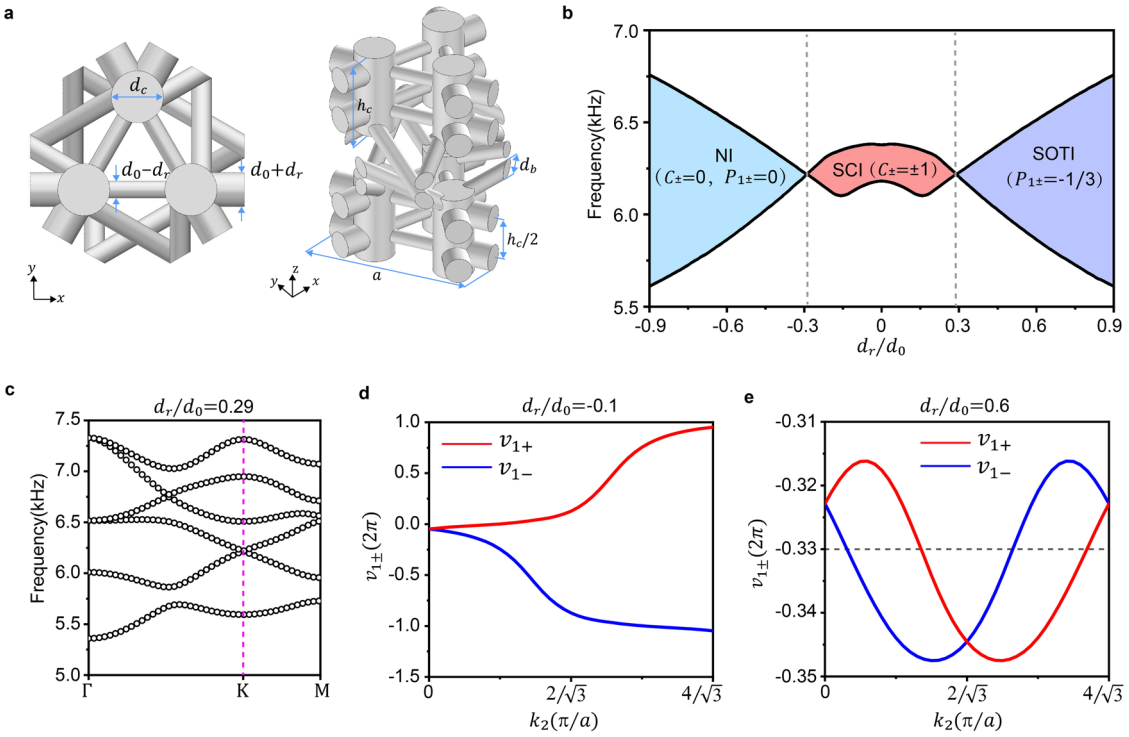

Fig. 2 Phase diagram and topological properties in the acoustic variable-order topological insulator. a Unit cell of the phononic crystal (PC) with top and side views. **b** Phase diagram with bulk gap of the dipole modes, including normal insulator (NI), spin-Chern insulator (SCI) and second-order TI (SOTI). **c** Gapless bulk dispersion of the dipole modes for the parameter $d_r/d_0 = 0.29$. **d** and **e** Calculated the spin-polarized Berry phases v_{1+} (spin-up) and v_{1-} (spin-down) as a function of k_2 for the parameters $d_r/d_0 = -0.1$ and 0.6, respectively.

the different phases with bulk gaps are shown in Supplementary Note 2. To confirm the topological nature of the bulk gap, we calculate the spin-polarized Berry phases $v_{1\pm}$ along the loop $k_1 \in \left[0, 4\pi/\sqrt{3}a\right]$ as a function of k_2. Due to the dipole modes, we use the pressure fields at the center of the circle at $3h_c/4$ height the six cavities in a primary cell to construct the normalized wavefunctions. As shown in Fig. 2d, for the parameter $d_r/d_0 = -0.1$ in the SCI phase, the Berry phase for the spin-up (spin-down) polarization winds 2π (-2π) when k_2 runs a loop from 0 to $4\pi/\sqrt{3}a$, leading to $C_+ = 1$ ($C_- = -1$). In Fig. 2e, for $d_r/d_0 = 0.6$ in the SOTI phase, the Berry phases for both the spin-up and spin-down polarizations wind zero, giving rise to $C_\pm = 0$. However, the spin-polarized bulk polarizations $P_{1\pm} = -1/3$, obtained by integrating $v_{1\pm}$ over k_2, as shown by the dashed gray line. For the NI phase, $C_\pm = 0$ and $P_{1\pm} = 0$. These results confirm the PC hosts the topological phase transition between the SCI and SOTI phases, same to the lattice model.

For the acoustic SCI phase, non-zero spin-Chern numbers guarantee a pair of helical edge states on the boundaries of a PC ribbon. To verify it experimentally, we take parameter $d_r/d_0 = -0.1$, and fabricate a sample of 21×7 unit cells using 3D printing technology with resin materials DSM IMAGE8000. The sample has two different configurations of boundary, which is formed by triangles with tube diameter $d_0 - d_r$, as illustrated in Fig. 3a–d. The projected dispersions along the k_x direction are shown in Fig. 3e and f, corresponding to the top and bottom boundaries, respectively. Color maps denote the experimental results obtained from the Fourier transform of the sound pressure field in the cavity on the boundaries. Dots denote the simulated results calculated by COMSOL Multiphysics with $\rho = 1.3\text{kg/m}^3$ and $v = 346\text{m/s}$. For both two different boundaries, there are a pair of edge states with opposite group velocities emerge at the bulk gaps. The eigenfields for the helical edge states are shown in Supplementary Note 3. As shown in Fig. 3g, we measured the sound pressure field distributions excited by a point source at the top and bottom boundaries respectively, at $f = 6.225\text{kHz}$. A pair of edge states with positive and negative group velocities are excited simultaneously. Due to the thermal resistance effect of air, the intensity of sound fields at the boundaries decreases continuously during transmission. The agreement between the simulated and experimental results proves that the PC with parameter $d_r/d_0 = -0.1$ is the SCI.

For the acoustic SOTI phase, non-zero spin-polarized bulk polarizations lead to the corner states at the corners of a triangle-shaped PC. Figure 4a shows the triangle-shaped sample with $d_r/d_0 = 0.6$ bounded by triangles with tube diameter $d_0 - d_r$. The corresponding eigenfrequencies is calculated in Fig. 4b, where the orange circles show a pair of corner states with spin polarization located at each corner. Figure 4c shows the measured corner, edge and bulk normalized response spectra labeled by the orange, green and black areas. The positions of sources and probes are pointed by the yellow arrows in Fig. 4a. The response peaks are in good agreement with the simulated eigenfrequencies, demonstrating the existence of the corner modes. We further measure the pressure field distributions of the upper layer, corresponding to the bulk, edge, corner and bulk states for fixed frequencies, as shown in Fig. 4d. In this case, the source and probe are put at the same cavities. The visualized corner modes for $f = 6.470\,\text{kHz}$ reveal the PC with parameter $d_r/d_0 = 0.6$ is the SOTI. We also compare the edge state and corner state properties of different topological phases under the same excitation in Supplementary Notes 4 and 5.

Conclusions

In summary, we have reported variable-order TI, which hosts the topological phase transitions between the SCI and SOTI without

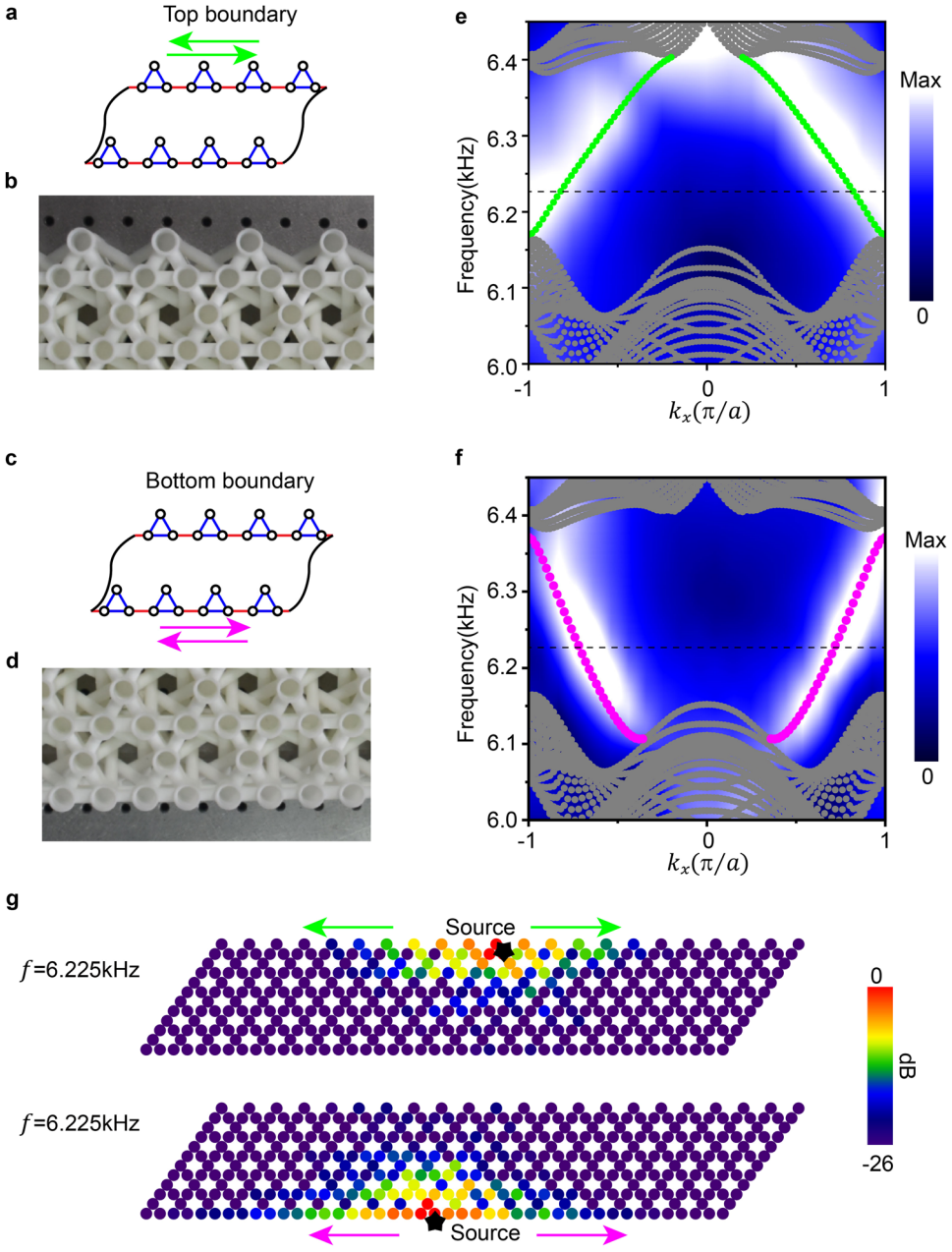

Fig. 3 Acoustic helical edge states in the spin-Chern insulator phase. Schematic and photo of (**a** and **b**), the top boundary and (**c** and **d**), the bottom boundary for a phononic crystal (PC) ribbon. Green (pink) arrows represent a pair of edge states counterpropagating along the top (bottom) boundary. **e** and **f** Projected dispersions of the PC ribbon for the top and bottom boundaries, respectively. Gray dots show the simulated bulk modes, while the green and pink dots represent the simulated edge modes. Color maps denote the experimental data. **g** Measured sound field distributions excited at top and bottom boundaries, respectively. Color map denotes the intensity of measured sound fields.

breaking any symmetry. The topological property of SCI is described by spin-Chern number, while that of SOTI is originated from quantized bulk polarizations. The acoustic 1D helical edge states in the SCI phase and the 0D corner states in the SOTI phase are evidently observed. Unlike the phase transitions in the previous works breaking symmetries[40–46], and the so-called boundary-obstructed topological phases[47,48], the transition here between the first-order and second-order TIs occurs still at the bulk gap closing without breaking symmetries. It is desirable to explore a simple method to adjust the interactions of hopping and show the phase transition in a single PC sample.

Methods

Simulations. All of the numerical simulations are performed by COMSOL Multiphysics. The parameters for the filling air in our systems are the mass density $\rho = 1.3\,\mathrm{kg\,m^{-3}}$ and sound velocity $v = 346\,\mathrm{m\,s^{-1}}$. The hard boundary conditions set in the simulations are easy to realize in the air acoustic system, due to a huge acoustic impedance mismatch between air and many materials, i.e., 3D-printed resin samples and so on.

Experiments. All the experimental measuring devices are composed of a headphone with a diameter of 6 mm (generate acoustic waves), a microphone probe with a diameter of 1.5 mm (measure the acoustic pressure fields), and a network analyzer Keysight 5061B (send and record the acoustic signals). The PC samples

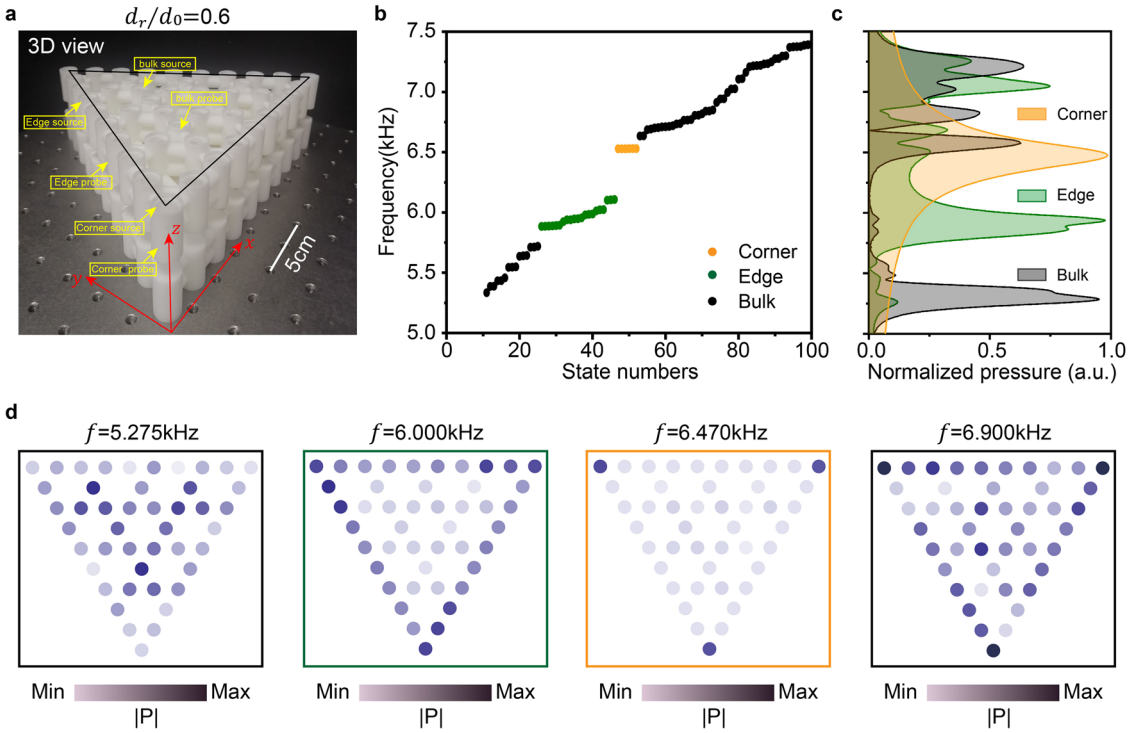

Fig. 4 Acoustic corner states in the second-order topological insulator phase. a Photo of triangle-shaped phononic crystal (PC) with $d_r/d_0 = 0.6$. **b** Simulated eigenfrequency of the triangle-shaped PC. Six corner states exist in the band gap. **c** Measured corner, edge and bulk response spectra as functions of frequency. **d** Measured pressure fields of lower bulk, edge, corner and higher bulk states. Color maps denote the magnitudes of the sound pressure |P|.

shown in the main text are prepared by 3D printing technology with resin materials DSM IMAGE8000. The parallelogram-shaped sample with 21×7 unit cells shown in Fig. 3 is used for measuring the SCI phase. At this time, the sound source is placed in a cavity in the middle of the sample boundaries, and the probe measure the sound pressure field distribution of all the cavities on the boundaries. The helical edge states are obtained by performing the Fourier transformations along the x directions. The triangle-shaped sample shown in Fig. 4a is used for measuring the SOTI phase. For the response spectra of bulk, edge and corner, the positions of sound source and probes are marked by yellow arrows in Fig. 4a. For the measurement of field distributions, the sound source and probe are located in the same cavity.

Data availability

The data that support the plots within this paper and other findings of this study are available from the corresponding author upon reasonable request.

Code availability

The Matlab code that support this study can be accessed from the corresponding author upon reasonable request.

Received: 29 December 2022; Accepted: 5 June 2023;
Published online: 19 June 2023

References

1. Bansil, A., Lin, H. & Das, T. Colloquium: Topological band theory. *Rev. Mod. Phys.* **88**, 021004 (2016).
2. Chiu, C.-K., Teo, J. C. Y., Schnyder, A. P. & Ryu, S. Classification of topological quantum matter with symmetries. *Rev. Mod. Phys.* **88**, 035005 (2016).
3. Ozawa, T. et al. Topological photonics. *Rev. Mod. Phys.* **91**, 015006 (2019).
4. Zhang, X., Xiao, M., Cheng, Y., Lu, M.-H. & Christensen, J. Topological sound. *Commun. Phys.* **1**, 97 (2018).
5. Ma, G., Xiao, M. & Chan, C. T. Topological phases in acoustic and mechanical systems. *Nat. Rev. Phys.* **1**, 281 (2019).
6. Klitzing, K. V., Dorda, G. & Pepper, M. New Method for High-Accuracy Determination of the Fine-Structure Constant Based on Quantized Hall Resistance. *Phys. Rev. Lett.* **45**, 494 (1980).
7. Haldane, F. D. M. Model for a Quantum Hall Effect without Landau Levels: Condensed-Matter Realization of the "Parity Anomaly". *Phys. Rev. Lett.* **61**, 2015 (1988).
8. Kane, C. L. & Mele, E. J. Z_2 Topological Order and the Quantum Spin Hall Effect. *Phys. Rev. Lett.* **95**, 146802 (2005).
9. Bernevig, B. A., Hughes, T. L. & Zhang, S.-C. Quantum Spin Hall Effect and Topological Phase Transition in HgTe Quantum Wells. *Science* **314**, 1757 (2006).
10. Yang, Y. et al. Time-Reversal-Symmetry-Broken Quantum Spin Hall Effect. *Phys. Rev. Lett.* **107**, 066602 (2011).
11. Deng, W. et al. Acoustic spin-Chern insulator induced by synthetic spin-orbit coupling with spin conservation breaking. *Nat. Commun.* **11**, 3227 (2020).
12. Li, H., Sheng, L. & Xing, D. Y. Connection of Edge States to Bulk Topological Invariance in a Quantum Spin Hall State. *Phys. Rev. Lett.* **108**, 196806 (2012).
13. Yu, R. et al. Quantized Anomalous Hall Effect in Magnetic Topological Insulators. *Science* **329**, 61 (2010).
14. Li, H., Sheng, L. & Xing, D. Y. Quantum phase transitions in ultrathin films of three-dimensional topological insulators in the presence of an electrostatic potential and a Zeeman field. *Phys. Rev. B* **85**, 045118 (2012).
15. Chang, C.-Z. et al. Experimental Observation of the Quantum Anomalous Hall Effect in a Magnetic Topological Insulator. *Science* **340**, 167 (2013).
16. Zhang, F., Kane, C. L. & Mele, E. J. Surface State Magnetization and Chiral Edge States on Topological Insulators. *Phys. Rev. Lett.* **110**, 046404 (2013).
17. Song, Z., Fang, Z. & Fang, C. $(d-2)$ Dimensional Edge States of Rotation Symmetry Protected Topological States. *Phys. Rev. Lett.* **119**, 246402 (2017).
18. Langbehn, J., Peng, Y., Trifunovic, L., von Oppen, F. & Brouwer, P. W. Reflection-Symmetric Second-Order Topological Insulators and Superconductors. *Phys. Rev. Lett.* **119**, 246401 (2017).
19. Schindler, F. et al. Higher-order topological insulators. *Sci. Adv.* **4**, eaat0346 (2018).
20. Benalcazar, W. A., Bernevig, B. A. & Hughes, T. L. Quantized electric multipole insulators. *Science* **357**, 61 (2017).
21. Fruchart, M. & Vitelli, V. Waves cornered. *Nature* **555**, 318 (2018).
22. Ezawa, M. Higher-Order Topological Insulators and Semimetals on the Breathing Kagome and Pyrochlore Lattices. *Phys. Rev. Lett.* **120**, 026801 (2018).
23. Zhang, X. et al. Second-order topology and multidimensional topological transitions in sonic crystals. *Nat. Phys.* **15**, 582 (2019).
24. Peterson, C. W., Benalcazar, W. A., Hughes, T. L. & Bahl, G. A quantized microwave quadrupole insulator with topologically protected corner states. *Nature* **555**, 346 (2018).
25. Mittal, S. et al. Photonic quadrupole topological phases. *Nat. Photon.* **13**, 692 (2019).
26. Chen, X.-D. et al. Direct Observation of Corner States in Second-Order Topological Photonic Crystal Slabs. *Phys. Rev. Lett.* **122**, 233902 (2019).

27. Xie, B.-Y. et al. Visualization of Higher-Order Topological Insulating Phases in Two-Dimensional Dielectric Photonic Crystals. *Phys. Rev. Lett.* **122**, 233903 (2019).
28. Serra-Garcia, M. et al. Observation of a phononic quadrupole topological insulator. *Nature* **555**, 342 (2018).
29. Ni, X., Weiner, M., Alù, A. & Khanikaev, A. B. Observation of higher-order topological acoustic states protected by generalized chiral symmetry. *Nat. Mater.* **18**, 113 (2019).
30. Xue, H., Yang, Y., Gao, F., Chong, Y. & Zhang, B. Acoustic higher-order topological insulator on a kagome lattice. *Nat. Mater.* **18**, 108 (2019).
31. Qi, Y. et al. Acoustic Realization of Quadrupole Topological Insulators. *Phys. Rev. Lett.* **124**, 206601 (2020).
32. Yang, Y. et al. Hybrid-Order Topological Insulators in a Phononic Crystal. *Phys. Rev. Lett.* **126**, 156801 (2021).
33. Imhof, S. et al. Topolectrical-circuit realization of topological corner modes. *Nat. Phys.* **14**, 925 (2018).
34. Serra-Garcia, M., Süsstrunk, R. & Huber, S. D. Observation of quadrupole transitions and edge mode topology in an LC circuit network. *Phys. Rev. B* **99**, 020304(R) (2019).
35. Wu, J. et al. Observation of corner states in second-order topological electric circuits. *Phys. Rev. B* **102**, 104109 (2020).
36. Yang, Z.-Z., Li, X., Peng, Y.-Y., Zou, X.-Y. & Cheng, J.-C. Helical Higher-Order Topological States in an Acoustic Crystalline Insulator. *Phys. Rev. Lett.* **125**, 255502 (2020).
37. Xie, B. et al. Higher-order quantum spin Hall effect in a photonic crystal. *Nat. Commun.* **11**, 3768 (2020).
38. Lin, Z.-K., Wu, S.-Q., Wang, H.-X. & Jiang, J.-H. Higher-Order Topological Spin Hall Effect of Sound. *Chin. Phys. Lett.* **37**, 074302 (2020).
39. Zhang, X., Liu, L., Lu, M.-H. & Chen, Y.-F. Valley-Selective Topological Corner States in Sonic Crystals. *Phys. Rev. Lett.* **126**, 156401 (2021).
40. Huang, J. et al. Room-Temperature Topological Phase Transition in Quasi-One-Dimensional Material Bi_4I_4. *Phys. Rev. X* **11**, 031042 (2021).
41. Wang, B., Zhou, X., Lin, H. & Bansil, A. Higher-order topological insulator phase in a modified Haldane model. *Phys. Rev. B* **104**, L121108 (2021).
42. Ren, Y., Qiao, Z. & Niu, Q. Engineering Corner States from Two-Dimensional Topological Insulators. *Phys. Rev. Lett.* **124**, 166804 (2020).
43. Chen, C. et al. Universal Approach to Magnetic Second-Order Topological Insulator. *Phys. Rev. Lett.* **125**, 056402 (2020).
44. Huang, X. et al. Acoustic higher-order topology derived from first-order with built-in Zeeman-like fields. *Sci. Bull.* **67**, 488 (2022).
45. Zheng, L.-Y. & Christensen, J. Dirac Hierarchy in Acoustic Topological Insulators. *Phys. Rev. Lett.* **127**, 156401 (2021).
46. Yang, L. et al. Observation of Dirac Hierarchy in Three-Dimensional Acoustic Topological Insulators. *Phys. Rev. Lett.* **129**, 125502 (2022).
47. Khalaf, E., Benalcazar, W. A., Hughes, T. L. & Queiroz, R. Boundary-obstructed topological phases. *Phys. Rev. Res.* **3**, 013239 (2021).
48. Du, J., Li, T., Fan, X., Zhang, Q. & Qiu, C. Acoustic Realization of Surface-Obstructed Topological Insulators. *Phys. Rev. Lett.* **128**, 224301 (2022).

Acknowledgements

This work is supported by the National Key R&D Program of China (Nos. 2022YFA1404500, 2022YFA1404900, 2018YFA0305800), National Natural Science Foundation of China (Nos. 11890701, 11974120, 11974005, 12074128, 12222405, 12247169), and Guangdong Basic and Applied Basic Research Foundation (Nos. 2019B151502012, 2021B1515020086, 2022B1515020102).

Author contributions

W.D. and Z.L. conceived the original idea. Y.Y., W.D., and J.L. did the theoretical analysis and designed the structures. Y.Y., H.S., and X.H. performed the experiments. Z.L. supervised the project. All authors participated in discussions and reviewed the paper.

Competing interests

The authors declare no competing interests.

Additional information

Supplementary information The online version contains supplementary material available at https://doi.org/10.1038/s42005-023-01261-6.

Correspondence and requests for materials should be addressed to Weiyin Deng or Zhengyou Liu.

Peer review information *Communications Physics* thanks Xue-Feng Zhu and the other, anonymous, reviewer(s) for their contribution to the peer review of this work. A peer review file is available.

Reprints and permission information is available at http://www.nature.com/reprints

Publisher's note Springer Nature remains neutral with regard to jurisdictional claims in published maps and institutional affiliations.